Synthesis and characterization of $\delta/\gamma - NbN$ for SRF cavity application and vortices study in EP Nb superconductor

Supervisor: Mattia Checchin
Co-Supervisor: Martina Martinello
Fermi National Accelerator Laboratory
Technical Division SRF Group

Stefano Trivini
University of Padova

October 5, 2017

1 Introduction

Superconducting Radio Frequency (SRF) cavities (fig.1) are a fundamental building block of high energy particles accelerators. They're purpose is to give energy to charged particles accelerating them. The main advantage of using superconducting materials instead of normal conducting ones is the lower power loss by joule effect. This advantage overcomes the power consumption needed by the cryoplant to keep the SRF cavities at a temperature of $\sim$2 K. In continuous operation the total power consumption is about 300 times lower for the SRF technology with respect to the normal-conducting one[1].

Nowadays the main SRF technology is based on Niobium (Nb), that is the element with the highest T_c (9,25 K) and has mechanical properties that allows shaping and welding, even in complicated structures. After being formed Nb cavities go usually under Electro-Polishing (EP) treatment that consists in exposing the surface to an $HF - H_2SO_4$ mixture to smooth imperfections. The Quality Factor (Q) is used to characterize the performance of the cavity and it's defined as the ratio of the energy gain per rf period and dissipated power:

$$Q_0 = \frac{\omega U}{P_d} = \frac{\omega \mu_0 \int_\tau |\mathbf{H}^2| d\tau}{R_s \int_\Sigma |\mathbf{H}^2| d\Sigma} = \frac{g}{R_s} \tag{1}$$

where g is the geometrical factor and R_s is the surface resistance. A simple proportionality relation for the surface resistance in presence of rf field is a result of BCS theory[2]:

$$R_s \propto exp\left(- \frac{T_c}{T} \right) \tag{2}$$

where T_c is a material parameter of the superconductor. It's straightforward to notice that decreasing the T_c at constant T the quality factor increases.

The purpose of this program is to produce a 2-5 μm thick layer of $\gamma - \delta$NbN on Nb by mean of solid-gas reaction in a furnace. This treatment would increase T_c from

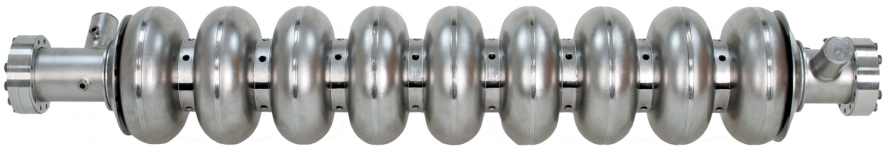

Figure 1: Nine cell 1.3 GHz Niobium Superconducting radio-frequency cavity.

9,25 K of Nb to 12-17 K of $\gamma - \delta$NbN increasing the quality factor by 10 times. The first treatments will be conducted on small Nb samples and the final purpose is to apply the technique to a 1.3 GHz SRF cavity. To do this we characterized different samples subjected to different treatments, in order to find the best conditions to grow NbN.

A parallel activity that we present is Magnetic Force Microscopy (MFM) imaging and analysis of vortices in Nb superconductor. The first purpose of the analysis is to observe vortices on the surface of type II superconductors and prove that the technique is sensible to surface effects (morphology and defects). The second purpose is to describe quantitatively the vortices using a model that simulates the magnetic field.

2 Basics of superconductivity

Superconductors materials are usually linked with the very low resistance to electron conduction at low temperatures. However the most important phenomena that characterizes superconductors is the Meissner-Ochsenfeld effect, in which the mate-

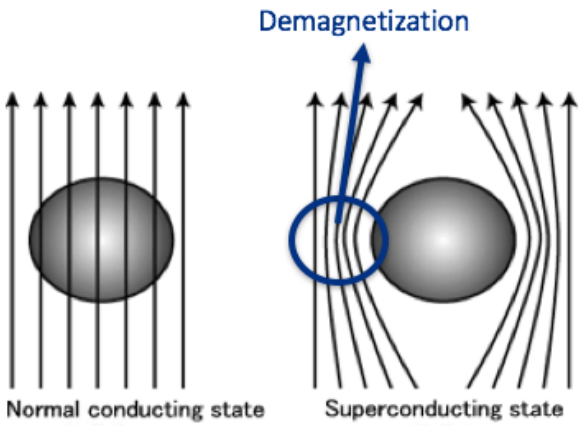

Figure 2: On the left the material is normal conducting and therefore is not expelling magnetic field. When the material is in the superconducting state the magnetic field is expelled. If the dimension of the material is finite in the field direction, the magnetic flux lines are concentrated and the field density increases locally. This is the demagnetization effect.

rial can be described as a perfect diamagnet and expels completely the magnetic flux lines. Anyway complete flux expulsion takes place only at small field, and when the dimension of the superconductor perpendicular to the field is small. When the latter condition is not true demagnetization locally occurs (there is concentration of magnetic flux lines and the magnetic flux density increases fig.2) and there is penetration of magnetic field with subsequent partial transition to normal state. The boundary between the normal and superconducting domains can have a positive or a negative energy, this defines if the superconductor behave respectively as a type I or type II superconductor[3].

2.1 Type I and Type II superconductors

The best way to detect superconductivity in some unknown sample is to measure its susceptibility, defined as follow:

$$\chi = \left.\frac{dM}{dH}\right|_{H=0} \tag{3}$$

If the sample is fully superconducting then $\chi = -1$ under a particular temperature called critical temperature (T_c). This susceptibility χ is defined in the limit of very weak external fields H. As the field becomes stronger it turns out that either one of two possible things can happen. The first case, called **type I superconductor**, is that the B field remains zero inside the material until suddenly the superconductivity is destroyed. The field where this happens is called critical field (H_c). In fig.3 is shown that for lower fields than H_c the magnetization obey at M=-H and then becomes suddenly zero (or very close to zero).

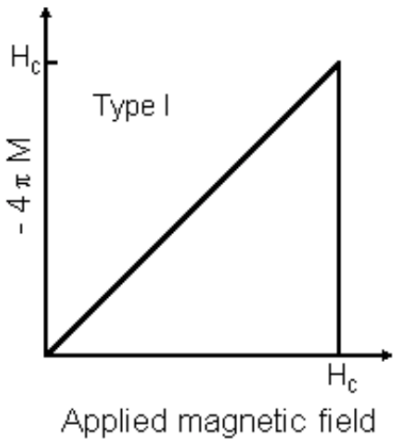

Figure 3: In a type I superconductor the magnetization is nearly zero when the applied field is higher than the critical field and the temperature is lower than the critical temperature. When the field becomes lower than the critical field the susceptibility turns to be -1.

In a type II superconductor there are two different critical fields, denoted H_{c1}, the **lower critical field**, and H_{c2} the **upper critical field**. For small values of H the Meissner effect again leads to $M = -H$ and there is no magnetic flux density inside the sample (B=0). However, in a type II superconductor, once the field exceeds

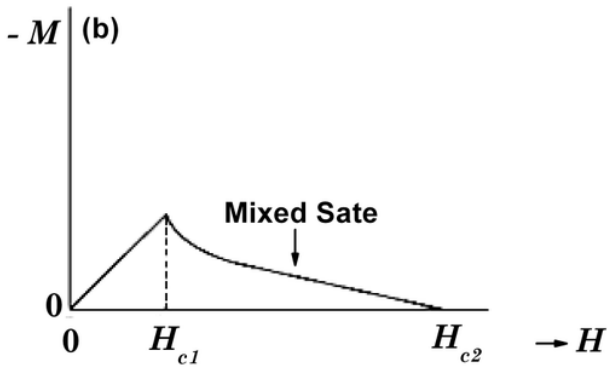

Figure 4: In the graph is reported the magnetization in function of the critical field for a type II superconductor. There are two critical fields: below H_{c1} the material has the same behavior of a type I SC, above H_{c1} the magnetization don't fall immediately to zero values but it decreases smoothly and it reaches zero at H_{c2}.

H_{c1}, magnetic flux does start to enter the superconductor. Upon further increasing the field H, B increases, until finally at H_{c2} the superconductivity is destroyed and M≈0 (fig.4). Abrikosov gave an explanation of the thermodynamic phase between H_{c1} and H_{c2}, he showed that the magnetic field can enter the superconductor in the form of **vortices**. Each vortex consists of a region of circulating super current around a small central core which has become normal metal[2]. Single vortices are stable because the boundary energy between normal conducting and superconducting domains is negative for $H_{c1} < H < H_{c2}$ and $T < T_c$. For $H < H_{c1}$ the boundary energy is positive, and so the system tends to minimize the energy collapsing the vortices in single domains.

3 Instrumentation

3.1 Treated Nb samples

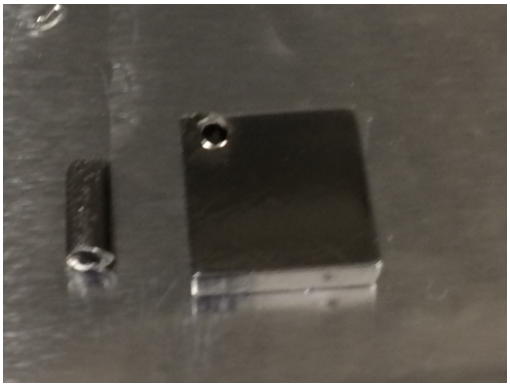

Figure 5: CaptionThe two kind of niobium samples treated, at left the cylinder for PPMS measurements and at right the 1x1 cm coupon for the other characterizations.

We used 2 kind of samples (see fig.5):

- Squared coupons 1x1 cm of Electro Polished (EP) Nb.
- Cylindric samples with height=6.7 mm and diameter=2.6 mm of EP Nb.

3.2 Furnace

The furnace used is a radiative heating furnace with molybdenum heating elements. The maximum temperature is 1000^oC and the pressure of N_2 is limited to a maximum of 50 mTorr to avoid the nitrogen contamination of the heating elements.

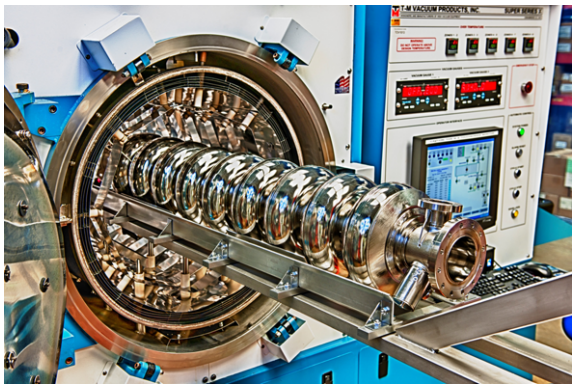

Figure 6: This is the furnace used for nitrogen treatments. There is a nine cell 1,3 GHz niobium SRF cavity in front of the chamber.

3.3 Scanning Electron Microscopy (SEM)

The Scanning Electron Microscope (SEM) is a microscope that works by scanning a focused beam of electrons on a sample of interest. The main SEM components include:

- Source of electrons
- Column down which electrons travel
- Electromagnetic lenses
- Electron chamber

Electrons are produced at the top of the column by a k-type filament, than they're accelerated down and they passes through a combination of lenses and apertures to produce a focused beam which hits the surface of the sample. The sample is mounted on a stage in the chamber area (fig.7) and both the column and the chamber are evacuated by a combination of pumps (low vacuum).

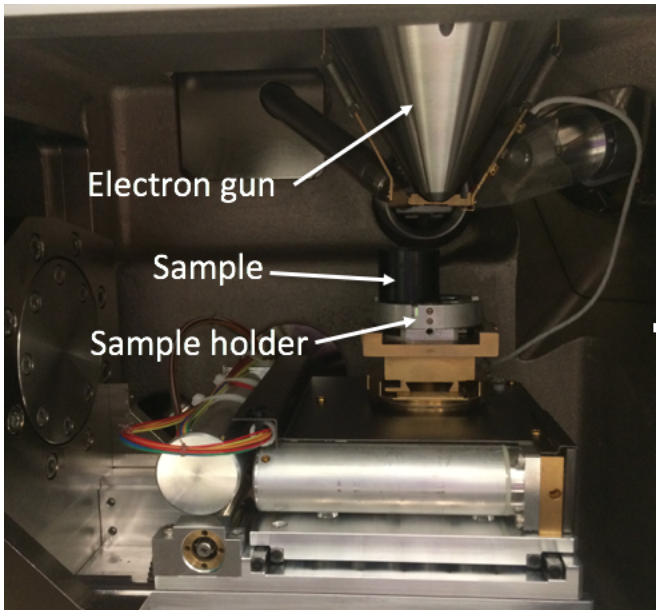

Figure 7: This is the inside of the low pressure SEM chamber, electrons comes from the electron gun and impinge the sample that is on a movable holder.

As result of the electron-sample interaction, a number of signals are produced:

- **Backscattered electrons**: these are high energy electrons which are scattered out of the specimen, losing only a small amount of energy.
- **Secondary electrons** these originate in the specimen itself, and have a much lower energy than the backscattered electrons.
- **X-rays**: these give information about the elemental composition of the sample (Energy Dispersive X-ray Spectrometry, EDS or EDX).

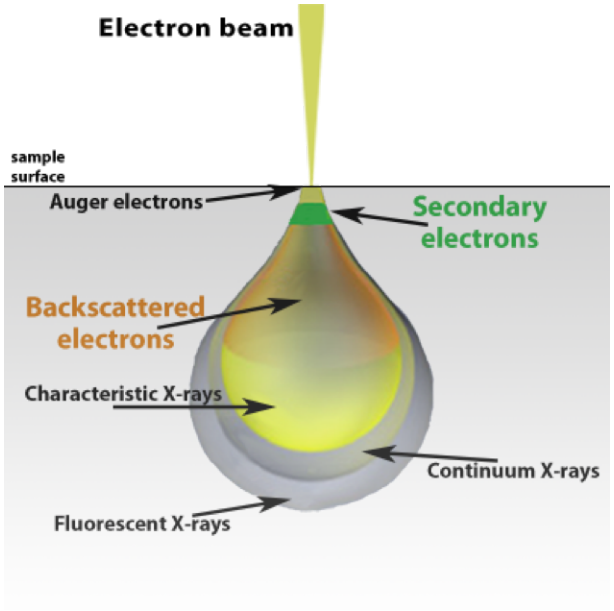

Figure 8: This is a sketch of the interaction volume of electrons in a SEM/EDX measurement. The bigger is the interaction volume the lower is the surface sensitivity.

The maximum resolution obtained in a SEM depends on multiple factors, like the electron spot size and the interaction volume of the electron beam with the sample. In fig.8 is schematized the interaction volume. This volume depends on the electron's energy due to the dependence on energy of the electron mean free path. In fig.9 is reported the electron mean free path as function of the electron energy, so, changing the energy, the interaction volume and the resolution can be tuned.

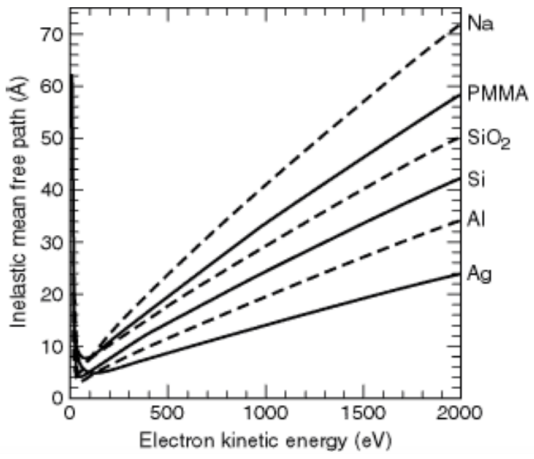

Figure 9: The graph shows the electron mean free path (EMFP) in different materials. In our SEM we can have from 8 to 30 KeV of electron energy, the EMPF grows for energy higher than 10eV .

The following are the main steps to obtain a good SEM image:

- Start from aperture 2 and focus at low magnification.
- Increase magnification in order to find structures of few microns.
- Adjust the position of the aperture with respect the beam using the wobbler tool.
- Find a circular structure and correct for the astigmatism aberration at high magnification.

3.4 Atomic-Magnetic Force Microscopy (AFM-MFM)

AFM provides a 3D profile of the surface at the nanoscale, by measuring forces between a sharp probe and surface at 0.2-10 nm probe-sample separation. The probe is supported on a flexible cantilever that can be set into oscillation by a piezoelectric tube. The amount of force between the probe and the sample is dependent on the spring constant (k) of the cantilever and the distance between the probe and the sample surface.

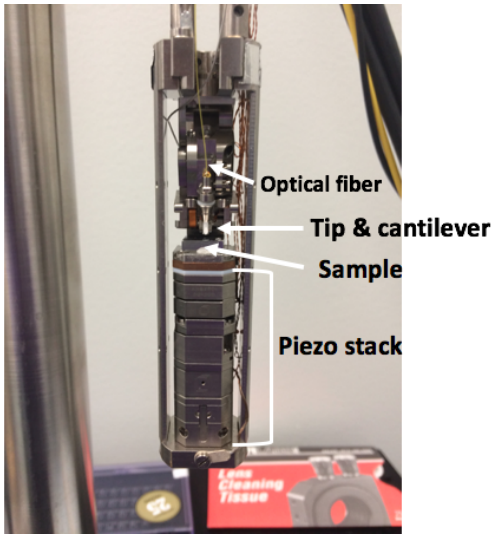

Figure 10: This is the core of the AFM-MFM instrument. The sample is put on a stack of piezoelectric actuators, the tip is between the optic fiber and the sample.

In our setup (attoAFM/MFM Ixs) the sample is moved with respect to the tip through a stack of piezoelectric actuators (fig.10). The bending of the tip is measured with an optical fiber based interferometer. A laser beam illuminates a cavity built up from the end-face of the fiber and the back- of the cantilever. The light reflected back from these surfaces gives rise to interferences that can be measured by a detector. In fig.11 is reported the interference signal, the periodicity of the signal corresponds to half the wavelength of the laser source. Hence, the system can be easily calibrated and a measured voltage difference can be translated into a height difference[4].

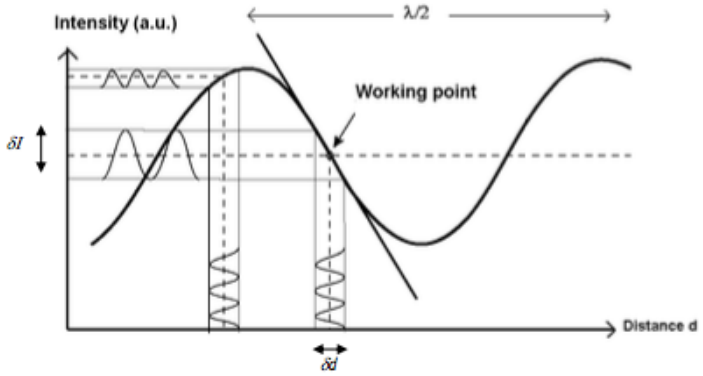

Figure 11: This is the interferogram created by the optical cavity, the working point is the point where the derivative of the interferogram is the highest (inflection points).

There are different working modes of AFM:

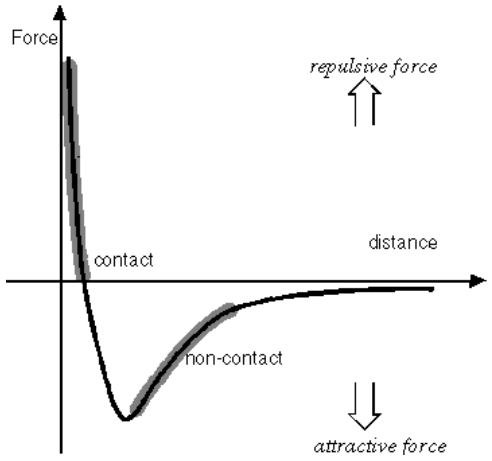

Figure 12: This is the force curve of the tip surface system. The tip interacts with Van Der Waals forces with the sample. The force can be attractive or repulsive, this depends on whether or not the tip-sample distance is greater or lower than the equilibrium distance (zero force and minimum energy).

- **Contact mode**: we are in the repulsive region of the force curve of tip-surface system (fig.12). The cantilever is not oscillating and is in direct contact with the sample, this results in a bending of the cantilever and hence to a compressive force onto the sample. Practically the cantilever position is adjusted such that the intensity of the interferogram is minimum, and then increasing the sample

height there is a bending of the cantilever that is kept constant by a feedback loop.

- **Non-contact mode**: we are in the attractive region of the force curve (fig.12). The cantilever is excited by the dither piezo at it's resonance frequency (fig.13). A lock-in amplifier measures the AC component of the photo-detected signal. As the cantilever approaches the sample, the oscillation amplitude drops rapidly with decreasing tip-sample distance. This signal serves as the input to a feed-back loop which maintains the cantilever oscillations at the set level by changing the z-position of the sample.

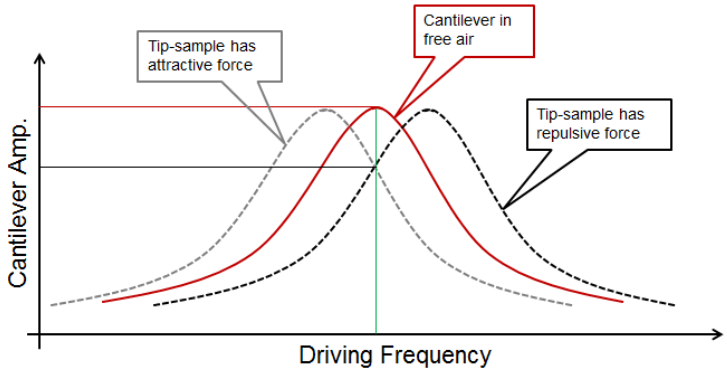

Figure 13: Looking at the frequency shift is one way to measure the differences in z position of the tip as a result of an interaction with the sample. The working frequency is the maximum of the resonance curve, if the sample get closer to surface the frequency increases and if the sample get closer the opposite.

Using a tip covered with cobalt is possible to map the magnetic field in a plane parallel to the surface. This is done using the dual pass mode: the topological (AFM) informations are gathered close to the surface, the magnetic (MFM) informations are gathered far from the surface (more than 50 nm). This is done in order to separate the topological features from the magnetic ones. The measurement is always based on measuring the cantilever oscillation amplitude, that changes depending on the magnetic force between the tip and the surface. The main part of the instrument (fig.10) can be placed in a dewar and a temperature of 2 K can be reached, this allows to study properties of superconductors

3.5 Physical Properties Measurement System (PPMS)

The Quantum Design PPMS is able to perform a variety of automated measurement in a temperature-field controlled system. The instrument is schemed in fig.14 and consists in a probe inserted in a dewar, the system is controlled by some hardware connected to a computer.

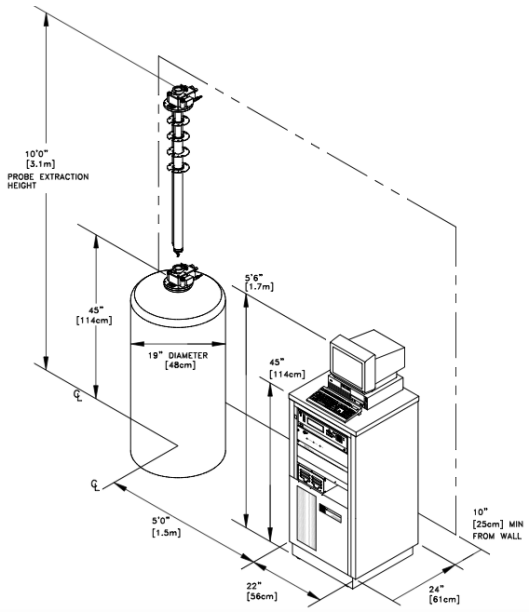

Figure 14: The main parts of the PPMS[5] are: the dewar, the control station and arm with the real instrument. The core of the instrument is at the extremity of the arm that goes in the dewar and it defines which measurement technique is used.

It's possible to do two different kind of measurements of the magnetic properties: **AC measurements** that yield information about magnetization dynamics and **DC measurements** where the sample magnetic moment is constant during the measurement time.

- **DC Magnetometry**: the magnetic moment of the sample is measured by induction technique, moving the sample relative to a set of measuring coils by vibration (Vibrating Sample Magnetometer, VSM)[6] or one-shot extraction. We used this configuration to extract hysteresis loops of Magnetization in function of applied magnetic field (fig.25).

- **AC Magnetometry**: in AC magnetic measurements, a small AC drive magnetic field is superimposed on the DC field, causing a time dependent moment in the sample. The field of the time-dependent moment induces a current in the measuring coils (fig.15), allowing measurement without sample motion. At very low frequencies, the measurement is similar to DC magnetometry and the induced AC moment is:

$$M_{AC} = \frac{dM}{dH} \cdot H_{AC} sin(\omega t) \tag{4}$$

where H_{AC} is the driving field, ω is the driving frequency, and $\chi = \frac{dM}{dH}$ is the slope of the $M(H)$ curve called the susceptibility. The advantage of the AC measurement with respect to DC is that AC is sensible to the slope of M(H), in fact small magnetic shifts can be detected even when the absolute M is large. At higher frequencies there could be a lag between the drive field and the magnetization and so the measurement yields two quantities: the magnitude of χ, and the phase shift ϕ relative to the drive signal. The phase shift indicates dissipative processes in the sample and with superconductors samples can be used to estimate the critical current (the maximum current that a superconductor can carry before becoming electrically resistive). In this work we used the AC configuration to estimate the critical temperature of a superconductive sample (fig.24). This can be done measuring the susceptibility at different temperatures, which magnitude is small for the normal state and -1 for the Meissner state (in SI measure system).

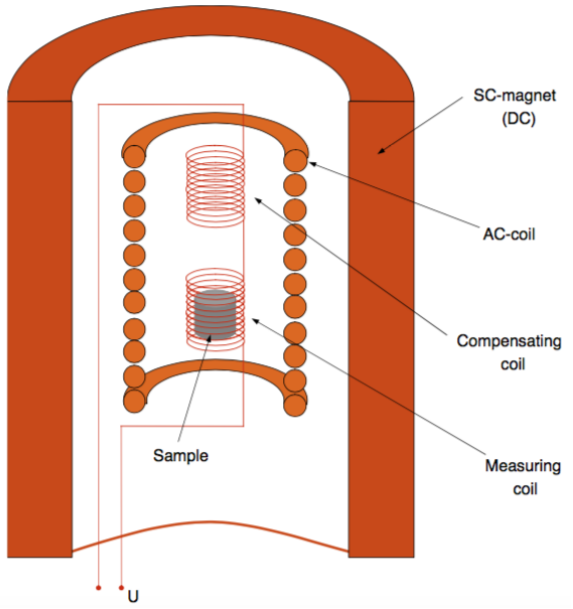

Figure 15: In the figure is schemed the coil configuration of the mutual inductance magnetometer in the PPMS-ACMS instrument.

3.6 Polishing for cross section samples

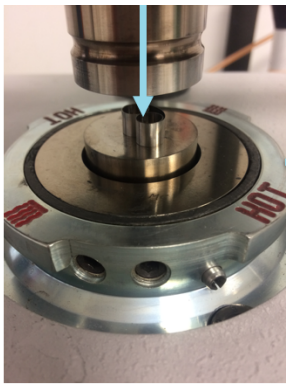

Figure 16: This is the main part of the embedding machine for the cross section measurements. On the stage there is one clip for holding the sample in place.

Embed the sample in the conducting polymer:

- Weight ≈38g of Konductomet powder.
- Grind the powder with the help of a blender (do not inhale Konductomet).
- Fix the sample with 2 clips and place it vertical on the stage of the embedding machine Simplimet 3000 (fig.16).
- Fill in the grinded powder and close the machine.
- The heating program should be already loaded, press the start button to begin the procedure.

Cut the Konductomet embedded sample with this precautions:

- Sharpen the saw using the sharpener.
- Make sure that the oil is touching the saw.

Figure 17: On the left there is the by-hand polishing machine, the grit of the paper is increasing from left to right. On the right there is a molded sample divided in section for the polishing.

Use Buehler Handmet 2 (fig.17):

- Divide the sample in 8 slices of 45^o using the engraver or the knife (fig.17).
- Start from grit 240, slide the sample with distilled water from top to bottom (not from bottom to top) ≈10 times for every 45^o division.
- Rinse with water and dry with a single sheet wipe.
- Look the sample with an optical microscope, switch to the next grit if you see all the scratches oriented in the same direction.

- Repeat for all grit types removing the used rub paper from the machine.

Figure 18: The polishing paper is sticked on the circular plate. The plate can spin and the sample is gently pressed on it by hand.

Here is possible to proceed 2 ways:

1. Use the rotating polishing machine(fig.18):
   - Find a 1200 and a 800 rub paper and stick the 800 on the machine.
   - Hold the sample pressed on the paper with one hand for 1-2 min and sprinkle water on the disk time to time while the disk is rotating.
   - Get off the sample before, and then turn off spinning.
   - Use the microscope to be sure that scratches left by 600 grit has disappeared.
   - Change the rub paper to 1200 and repeat from a).

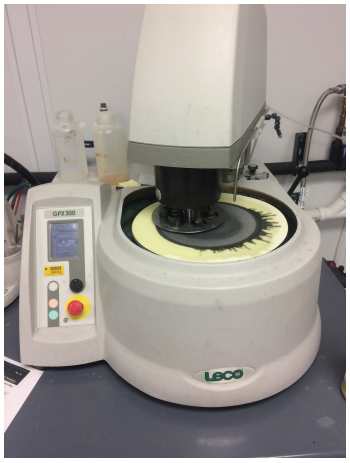

Figure 19: The samples are automatically holded and pressed on the polishing paper.

2. Use GPX 300 of machine (fig.19):
    - Place the paper on the green surface.
    - Sprinkle some $6\mu m$ diamond oil on the paper sheet.
    - Press grey button to approach the older to the paper sheet.
    - Place the samples, select the program and Press the green button.

Place the sample in the Vibromet (fig.20) being sure that the sample's surface is exposed from the holder and leave it overnight. If your sample is too short, use a spacer between the sample and the holder. The sample's surface at the microscope should be without any sign or scratches after Vibromet.

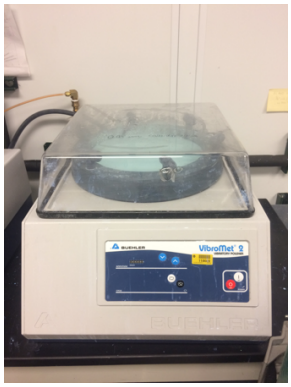

Figure 20: The sample has to be secured in a vibromet sample holder, than just immersed in the nanoparticle suspension facing down.

4 Experimentals

4.1 NbN synthesis

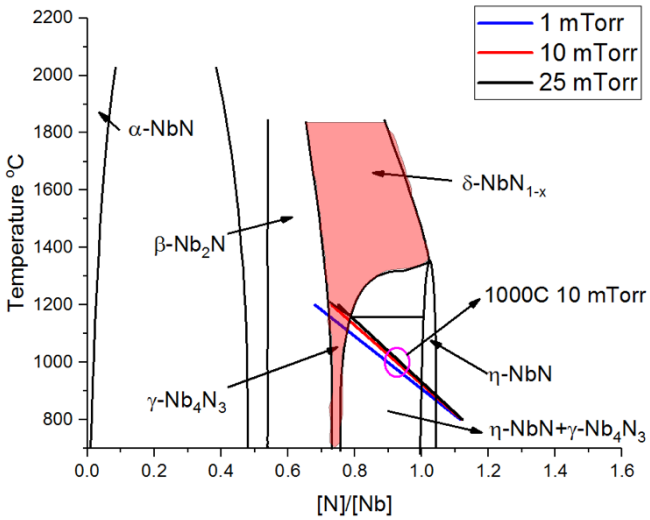

Figure 21: This is the phase diagram of the Nitrogen-Niobium system. The superconductive phase in which we are interested for are highlighted in red. The straight lines on the graph are calculated from eq.5 at different pressures.

In fig.21 is reported the partial phase diagram of the mixture Nitrogen-Niobium[7]. The phases present are[8]:

- $\alpha - NbN$: solid solution with concentration of nitrogen below 10%.
- $\beta - Nb_2N$: hexagonal phase non superconductive.
- $\eta - NbN$: hexagonal phase non superconductive.
- $\delta - NbN_{1-x}$: hexagonal phase superconductive with a T_c of 15-17 K.
- $\gamma - Nb_4N_{3\pm x}$: tetragonal phase with a T_c of 12-15 K.

Pure niobium has a T_c of 9.25 K, the purpose is to grow a layer of $\delta - NbN_{1-x}$ or $\gamma - Nb_4N_{3\pm x}$ (from this point called NbN for brevity) thicker than the penetration depth of the AC field.

During the treatment we can control the temperature of the furnace and the pressure of nitrogen in the chamber. In literature the synthesis of NbN is done at very high temperature and pressures (1600-2000 K, 30-100 bar), that are not suitable for cavity applications. In this work we are trying to produce a layer of NbN with milder conditions, using a furnace that can fit a 9 cell SRF cavity. To estimate how the pressure can influence the growth we used an empiric relation[7] that relates temperature, pressure and the atomic percentage of Nb and N:

$$\frac{[N]}{[Nb]} = 1.585 - 4.148 \cdot 10^{-4} \cdot T - 0.05176 ln(p_{N_2}) + 4.984 \cdot 10^{-5} \cdot T \cdot ln(p_{N-2}) \quad (5)$$

where p_{N_2} is the nitrogen pressure in bar, T the absolute temperature (K) and $\frac{[N]}{[Nb]}$ the atomic percentage of nitrogen and niobium in $\delta - NbN_{1-x}$. On the phase diagram are superimposed three of these curves calculated for 3 different pressures. Looking at the graph is straightforward that to obtain NbN a temperature of $\approx 1200^o$ is needed. The furnace used can reach only 1000^oC and so we will work in the coexistence region between $\gamma - NbN$ and $\eta - NbN$. So if the layer is formed, it's expected to be a mixture of the two phases.

Four run in furnace were done with 3 squared coupons and 1 cylinder for PPMS, before fluxing nitrogen the samples were baked at 800^oC for 3h to degas hydrogen:

- $T = 800^o$C, p_{N_2}25 mTorr and t=25min
- $T = 1000^o$C, p_{N_2}10 mTorr and t=2h
- $T = 1000^o$C, p_{N_2}50 mTorr and t=2h

4.2 Samples characterization

The samples has been characterize in order to look at morphology, stoichometry and superconducting properties.

4.2.1 Morphology

To look at the sample's surface morphology SEM and AFM can be done on squared coupons. With SEM we collected images with a maximum magnification of x11000. Top and cross-section images were measured, for the first it's interesting to see how the nitrides phases are distributed on the surface and for the latter, the presence of a surface layer of NbN was investigated. The advantage of AFM is that is possible to do quantitative measurement on z dimension of superficial structures.

4.2.2 Stoichometry

The stoichometry was measured by Energy Dispersive X-ray Spectrometry (EDX). Lowering the electrons's energy is possible to be more sensible to the surface composition. Anyway with the beam incident on the surface it's not possible to separate the contribution of different layers with 1-2μm width. To do so a cross section measurement was done. A coupon squared sample for every treatment condition was molded, cut and polished and looked at the SEM.

4.2.3 Superconductive properties

Two kind of measurements were possible: DC magnetometry ad AC susceptibility measurements. The first is sensible only to bulk properties and the second more to surface properties. Bulk equilibrium properties are extracted from the magnetization in function of the applied magnetic field.

The critical temperature measurement should be informative of the phases present in the sample, in dependance on the T_c we expect susceptibility detected transitions at different temperatures.

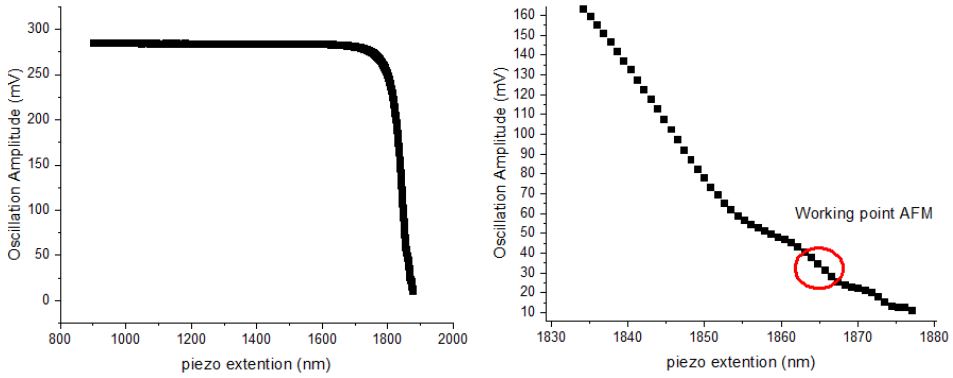

Figure 22: In the graph is reported the oscillation amplitude in function of the piezo extension. The choice of the working point sets the tip-sample distance.

4.3 MFM Vortex imaging

The samples analyzed were an EP Nb sample and a nitrogen treated sample (1000^{o}C 10 mTorr 2h). The objective was to obtain clear images varying the tip-sample distance. In this way we can use a theoretical model that describe the magnetic field of a vortex to estimate the penetration depth. The MFM measurement is done in non-contact mode, moreover the tip-sample distance must be greater than the one adopted in AFM because we want to separate the topological information from the magnetic information. To do the simulation an important parameter is needed, the tip-sample distance. To measure this parameter the following procedure was adopted: we changed the piezo voltage approaching the sample to the tip, when the tip is interacting with the sample the oscillation amplitude drops (fig.22), when the tip is very close to the sample, it's no more oscillating and this point has taken as the zero (fig.22). Than the working point is chosen, this means that the feedback loop keep the oscillation amplitude to a set value and this corresponds to fix the tip-sample distance (the piezo extension is calibrated). Than the MFM measurement is done with the dual pass, in this way a double scansion is done: one close to the sample for topology (AFM) and one far from the sample (30-100 nm) to collect only magnetic informations. The tip-sample distance is calculated adding the set point for AFM measurement (always 20nm) to the lifting up amount for MFM.

5 Results and Discussion

This section is divided in two parts: the first is about the nitrogen treatments for the NbN synthesis and the second is about vortex study with MFM measurements.

5.1 NbN synthesis

5.1.1 Starting material: electropolished niobium

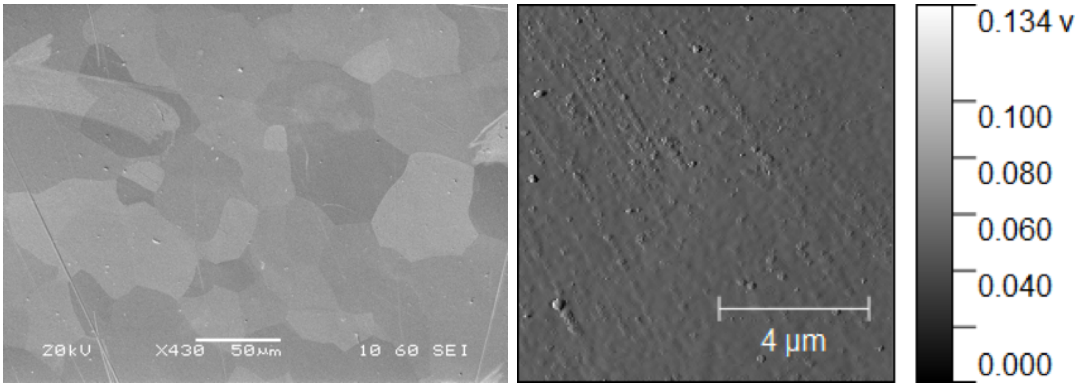

Figure 23: SEM (left) and AFM (right) images of EP Nb are reported. EP Nb sample is polycrystalline and the surface is flat, in the AFM image the features of the surface are oriented in one preferential direction. This is a consequence of the Electropolishing treatment.

As first thing we characterized niobium EP not treated with N_2, this is the starting point and it's the reference for morphology and superconducting properties. In fig.23 there is a SEM image with relatively low magnification, here we can see the crystalline domains with dimension from 10 to 50 microns. In fig.23 is reported an AFM image where is clear that the surface is flat and is presenting features with few nanometers lateral dimensions.

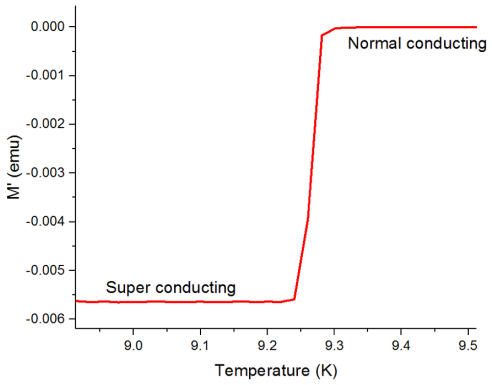

Figure 24: In the graph is shown a PPMS-ACMS measurement of the susceptibility in function of the temperature for EP Nb. The transition for niobium at 9,26 K is evident.

Looking at the superconducting properties turns out, as expected, that the critical temperature of EP Nb is $T_c = (9.26 \pm 0,01)$. This is deducible from the susceptibility measurement made with PPMS in ACSM mode In fig.24 datas are reported and is visible that for T greater than T_c the magnetization is close to zero and so is the susceptibility. Lowering T the transition towards superconducting phase occurs and the susceptibility becomes -1 (the y axis scale is not relevant, now just the offset is). Furthermore, with PPMS, the bulk magnetization loop is measured.

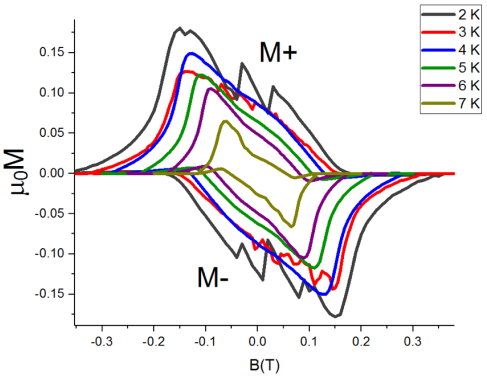

Figure 25: PPMS-DC Magnetometry curves for different temperatures are reported for EP Nb. The loops shows clearly that the magnetization process is irreversible and hysteresis is observed.

In fig.25 datas are reported, the magnetization of the sample is reported in function

of the applied magnetic field for different temperatures. Niobium is a type II superconductor, this is reflected in the irreversibility of the magnetization curve. To separate the reversible part of the loop, the following formula was used:

$$\mu_0 M_{rev} = \frac{\mu_0 M_+ + \mu_0 M_-}{2} \tag{6}$$

where M_+ and M_- are respectively the positive and the negative part of the magnetization loops. From the reversible curve (fig.26) the thermodynamic critical field H_c can be extracted, H_c is the critical field obtained describing the superconductor as a type I.

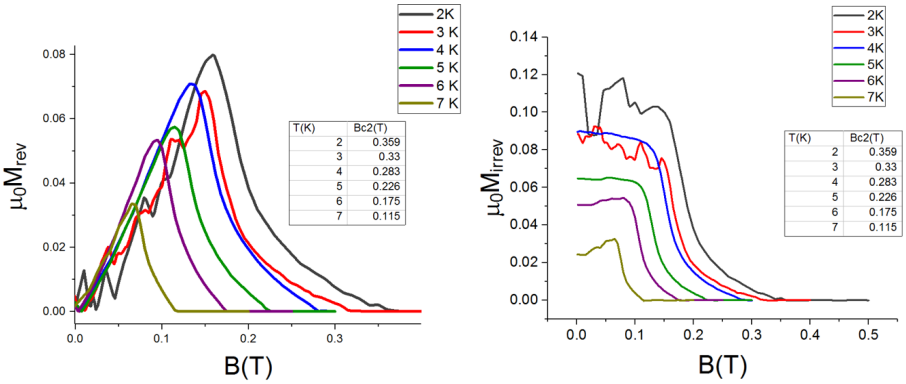

Figure 26: The curves are the reversible (left) and the irreversible (right) components of the magnetization loops in fig.25 calculated with eq.6 and eq.8.

The formula is the following:

$$B_c^2 = 2\mu_0 \int_0^{B_{c_2}} M_{rev}(B) dB \tag{7}$$

In fig.26 the values of B_c calculated were reported for different temperatures. To separate the irreversible part, the following formula was used:

$$\mu_0 M_{irrev} = \frac{\mu_0 M_+ - \mu_0 M_-}{2} \tag{8}$$

From the irreversible part the upper critical field B_{c2} can be calculated, that is the B field point where the magnetization goes to zero. The values are reported in fig.26 for different temperatures. The $B_c(T)$ and $B_{c2}(T)$ values obtained, are point of the

phase diagram H(T) of niobium that is reported in fig.27 (to convert from H to B was used $B = \mu_0 H$) .

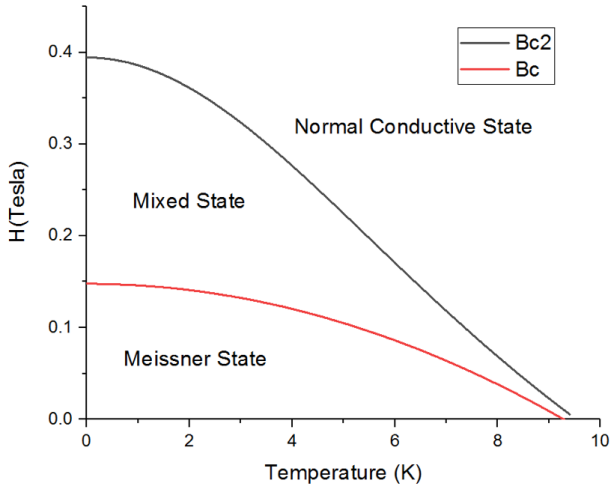

Figure 27: This is the phase diagram calculated with the critical fields values at different temperatures for EP Nb. The data were fitted with eq.eqphase1 and the critical fields at zero kelvin were extracted.

From this phase diagram B_c and B_{c2} were calculated fitting the data sets with the following empiric relations:

$$H_{c2}(T) = H_{c2}(0)\frac{1-(T/T_c)^2}{1+(T/T_c)^2} \qquad H_c(T) = H_c(0)[1-(T/T_c)^2] \tag{9}$$

Than the critical fields at zero temperature were used to estimate the Ginzburg-Landau parameter (k), che coherence length xi and the London penetration depth λ_L (all at 0K):

$$k(0) = \frac{B_{c2}(0)}{\sqrt{2}B_c(0)} \qquad \xi(0) = \sqrt{\frac{\hbar}{2eB_{c2}(0)}} \qquad \lambda_L(0) = k(0)\xi(0) \tag{10}$$

In fig.28 are reported the calculated parameters: the estimation of T_c has a big uncertainty, this is because we collected few points around T_c. A better estimation of T_c is obtained with ACMS measurement.

	Not corrected	Corrected
B_{c2}(0)(Tesla)	0.394±0.005	0.485±0.005
B_c(0)(Tesla)	0.148±0.005	0.182±0.005
T_c(K)	9.41±0.42	9.41±0.42
k(0)	1.89±0.07	1.89±0.07
λ_L(0)(nm)	54±2	49±2
ξ(0)(nm)	28.9±0.2	26.1±0.2

Figure 28: In the table are reported the parameters calculated with the DC magnetization measurement using eq.10 for Nb EP.

The sample is not infinitesimal in the field direction, so demagnetization effects occur. The demagnetization coefficient D can be calculated as follow for a cylindrical sample:

$$D = 1 - \frac{1}{1 + qa/b} \qquad q = \frac{4}{3\pi} + \frac{2}{3\pi} tanh\left(1.27\frac{b}{a} ln\left(1 + \frac{a}{b}\right)\right) \tag{11}$$

where a is the radius of the cylinder and b is the half of the height. With data in section 3.1 turns out that D=0,187. So to calculate the field locally felt by the sample we use:

$$H_{corrected} = \frac{H}{1 - D} \tag{12}$$

and than the other parameters has to be corrected (fig.28). The H_{c2} value for 100% pure Nb is 410 mT, the obtained value (485 mT) seems reasonable for our sample.

5.1.2 Sample 800°C 25mTorr 25min

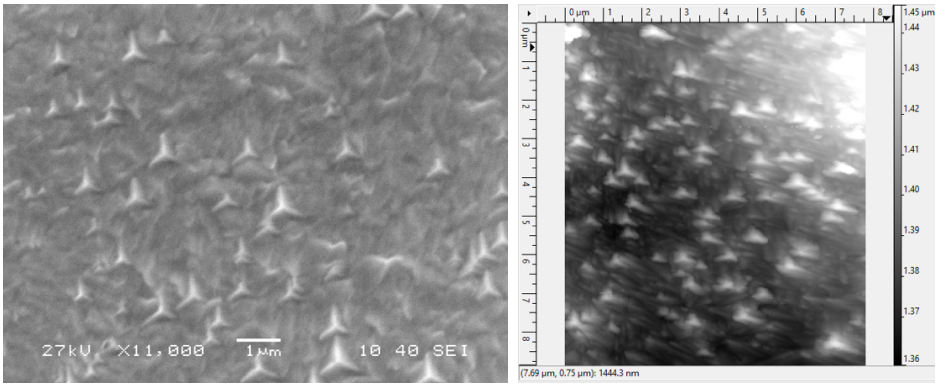

Figure 29: In figure are reported SEM (left) and AFM (right) images of the 800C 25 mTorr 25 min sample. The trigonal crystals of 1-2μm are $\beta - NbN$.

For identify the samples treated with nitrogen the notation Temperature, Nitrogen pressure and baking time will be used. This sample is not really part of this program, I used it to learn the various characterization techniques. In fig.29 is reported the surface morphology analysis made with SEM and AFM. On the surface are visible trigonal crystals that have been proven to be beta phase nitrides from Y. Trenikhina et al[9]. With AFM was found that the height of these structures is in between 30 and 70 nm.

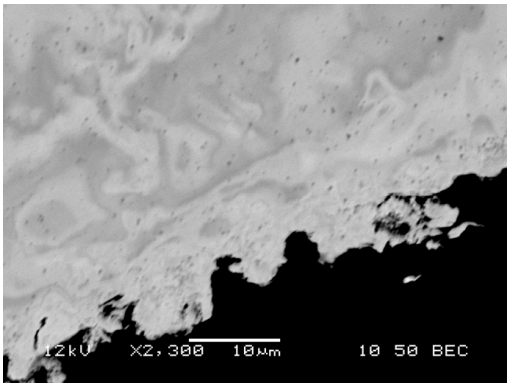

Figure 30: This is a SEM (backscattering electrons) cross section image of 800°C 25mTorr 25 min. A layer with different electronic contrast is visible. The Backscattered electrons are sensible to the structure of the material, the shadows in the image are indicative on the presence of strain in the lattice (channeling effects).

To investigate the surface properties a cross section measurement was done. A coupon squared sample was molded in conductive resin and looked at SEM. In fig.30 there is a SEM image of the cross section: the image was taken looking at the backscattered electrons. In the image is visible a different contrast for the surface layer, this could be an indication of the presence of nitrogen. In general in this work we weren't able to measure a significant quantity of nitrogen with EDX for all samples. A possible explanation is that the intense signals of carbon and oxygen cover the nitrogen signal (fig.37).

5.1.3 Sample 1000^oC 10mTorr 2h

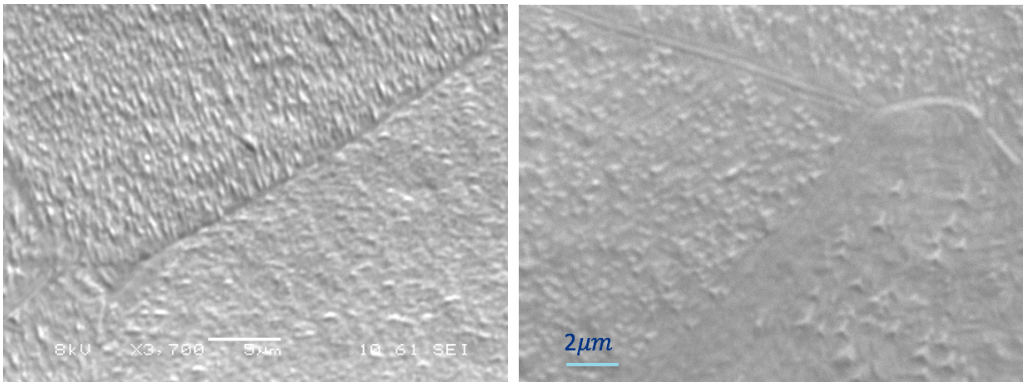

Figure 31: These are two SEM image of 1000^oC 10 mTorr 2h sample. The deposition is grain dependent, in some grains trigonal nitrides are found and in other grains a different kind of deposition is observed.

This sample is the first one of this work, 1000^oC is the highest temperature possible with our furnace. We chose the highest to be closer to the thermodynamic stability of $\delta - NbN$ that is stable over 1200^oC. In fig31 two SEM from top images are reported, the deposition is clearly grain dependent. The formation of the trigonal nitrides on some grains is evident, but in other grains the deposition seem to be more uniform on the surface. In fig.32 are reported the cross section measurements: only 2 faces of the sample, the one facing up during the process and one at side, presents layer with different electron contrast on surface. This could be again an indication of the presence of a nitrided layer, however the EDX measurement doesn't show a significative concentration of nitrogen in that layer.

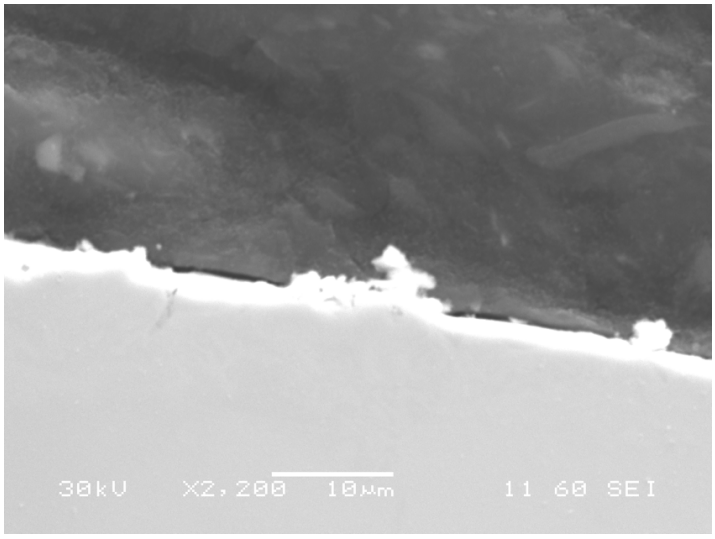

Figure 32: This is a SEM cross section image of 1000^{o}C 10 mTorr 2h sample. The black part is the epoxy resin used for cross section embedding, there is a white electron contrast layer of $\approx 1\mu m$ on the Nb surface.

In fig.33 is reported the PPMS measurement of T_c for the sample 1000^{o}C 10mTorr 2h, in the same graph are reported the bulk measurement (DC) and the surface sensitive measurement (AC). In the VMS DC measurement there is a single transition at $T_c \approx$ 9.2 K, in the ACMS measurement are visible three transitions at $T_c \approx 9.2/9.1/9.0$ K. This is an indication that we are modifying the surface properties, but no transition between 12 and 17 K was found and so in principle no stoichiometric layer of nitride is formed. Instead we created poor superconducting phases on the surface that have lower T_c than EP Nb.

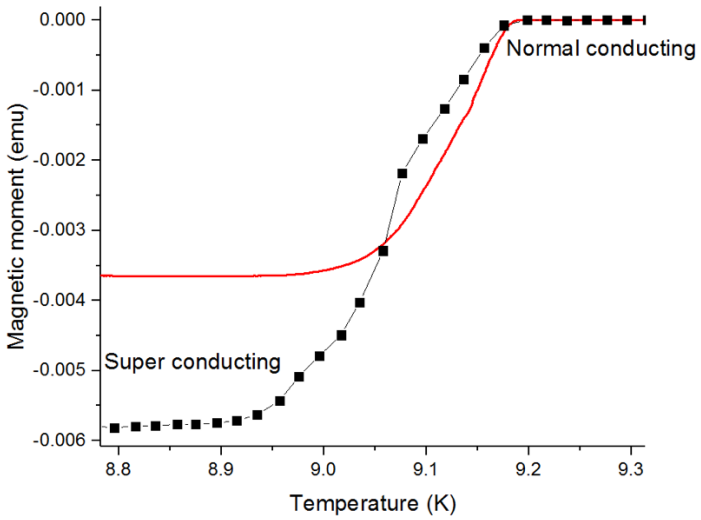

Figure 33: In the graph are reported the T_c measurement of the sample 1000^{o}C 10 mTorr 2h, in red the curve for bulk properties and in black the curve for surface properties. The red curve presents a single transition (typical for Bulk Nb) and the black curve presents three different transitions. This is an indication that the treatment modified the superconductive properties, but it has created poor superconducting phases.

5.1.4 Sample 1000^{o}C 50mTorr 2h

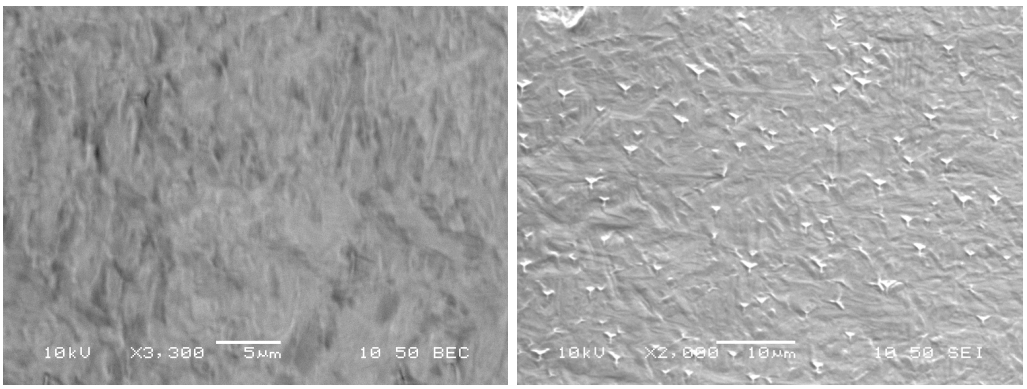

Figure 34: Two SEM images of the 1000^{o}C 50 mTorr 2h are reported: the formation of trigonal nitrides is grain-dependent.

In order to increment the thickness on the nitrided layer we increased the nitrogen pressure in the furnace by five times, keeping the other parameter fixed. In fig.34 are reported two SEM images and is again clear that the deposition is grain-dependent. Again the SEM cross section image is showing a layer with different contrast on two faces of the sample (again the one facing up and a side). The EDX measurement doesn't show a significative concentration of nitrogen in that layer.

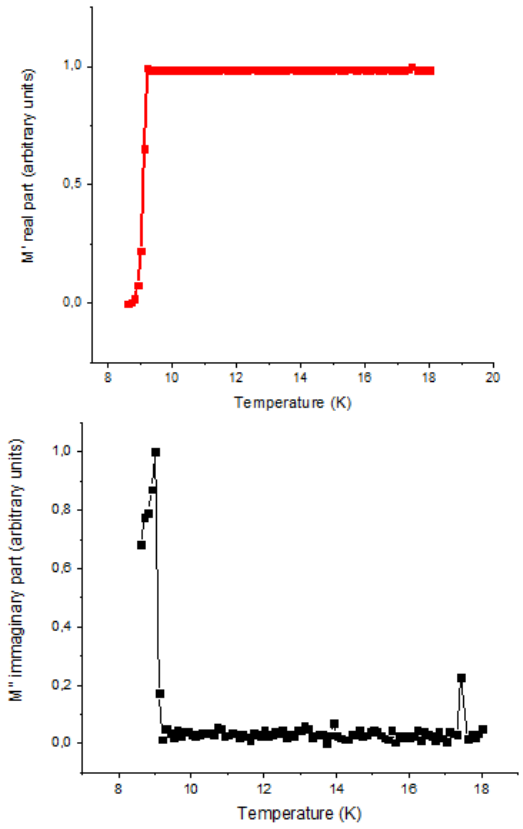

Figure 35: In the graphs is reported a rough scan of an ACMS measure for the 1000°C 50 mTorr 2h. In the imaginary part of the susceptibility there is the characteristic Nb signal at 9.2 K, at ≈17 K there is an oscillation that could be systematic. To be sure a precise scan in this range was done (fig.36).

In fig.35 is reported a rough scan of the ACMS susceptibility, between 17 and 18 K there is a signal in the imaginary part. It's a single point, so could be systematic, but that interval temperature is the one expected for $\delta - NbN$ and so we did a more precise measurement. In fig.36 are reported the ACMS measurements, we can see

clearly that there is no transition between 17 and 18K. In the 8K-10K range there is the known transition for EP Nb (9.25K) and a new transition at 8.33 K. The latter has never been observed for NbN, so it can be a new phase but further investigation should be done to recognize that phase.

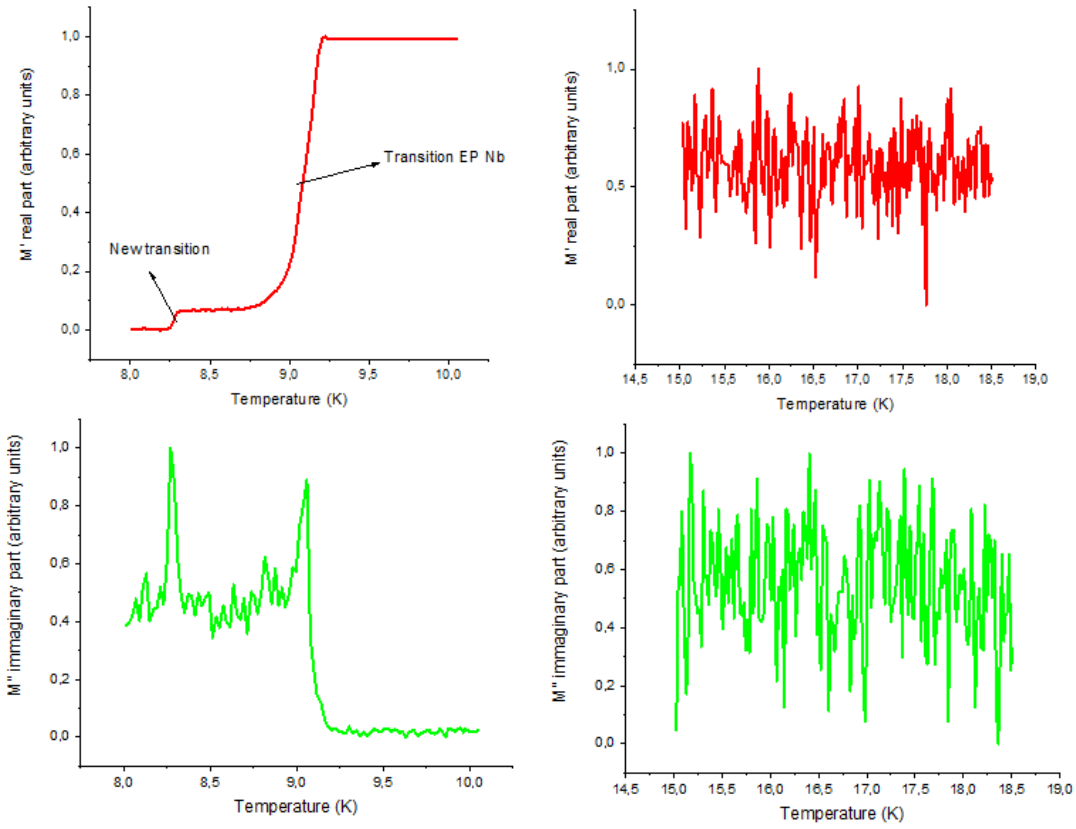

Figure 36: In the graphs are reported two precise scan of two ranges of the graph in fig.35. In the 15-18.5 K interval no transitions are visible. Instead in the 8-10 K interval two transitions are visible: one is the characteristic Nb transition(9.3 K), the other at 8.33 K it's not a common nitrides critical temperature. The magnetization variation for the second transition is lower, this is due to the surface character of the hypothetic phase produced.

5.1.5 Nitrogen detection by EDX

For all the samples we were not able to determine a significant concentration of nitrogen with the EDX (Energy Dispersive X-ray Spectrometry). In fig.37 an example of EDX spectra is reported: near the nitrogen signal there are carbon, oxygen and niobium that may cover the signal. Moreover the lateral and z resolution of the EDX is not very high and the nitrogen should be only in the very surface of the sample.

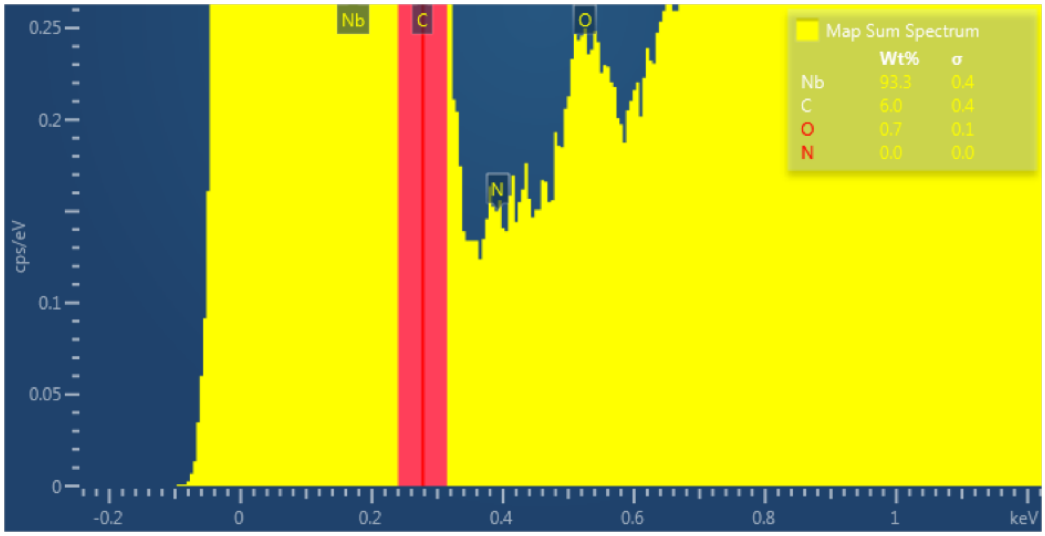

Figure 37: This is the EDX typical spectrum that is quite similar for all the nitrided samples analyzed. The nitrogen signal

5.2 MFM vortices study in superconductors

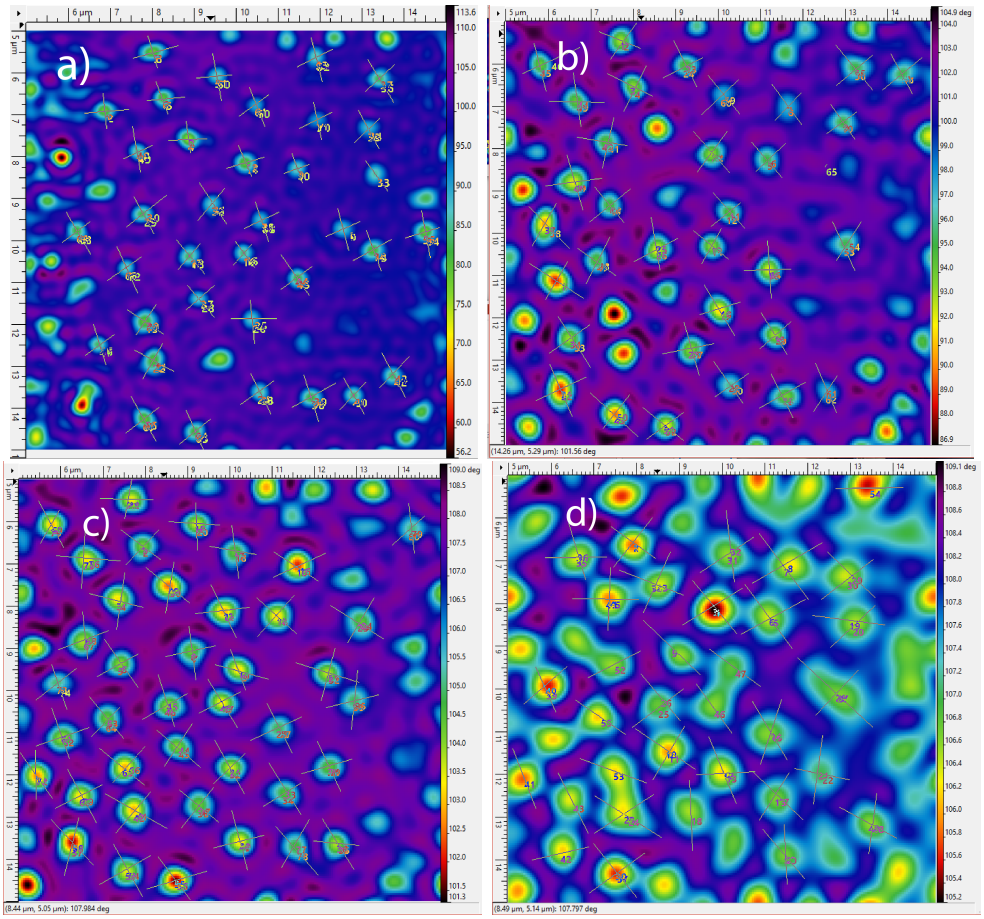

Figure 38: The MFM images for EP Nb are reported for different tip-surface distance. a) 50 nm, b) 70nm, c) 90 nm, d) 120 nm.

In MFM measurements the cobalt coated tip is sensible to the magnetic field variation. Anyway, to monitor the interaction, the observable used are the variation in amplitude and phase of the tip oscillation. In fig.38 there are MFM images of EP Nb, the color gradient scale is related to a phase variation. The phase variation is directly proportional to the second derivative of the magnetic field (eq.15).

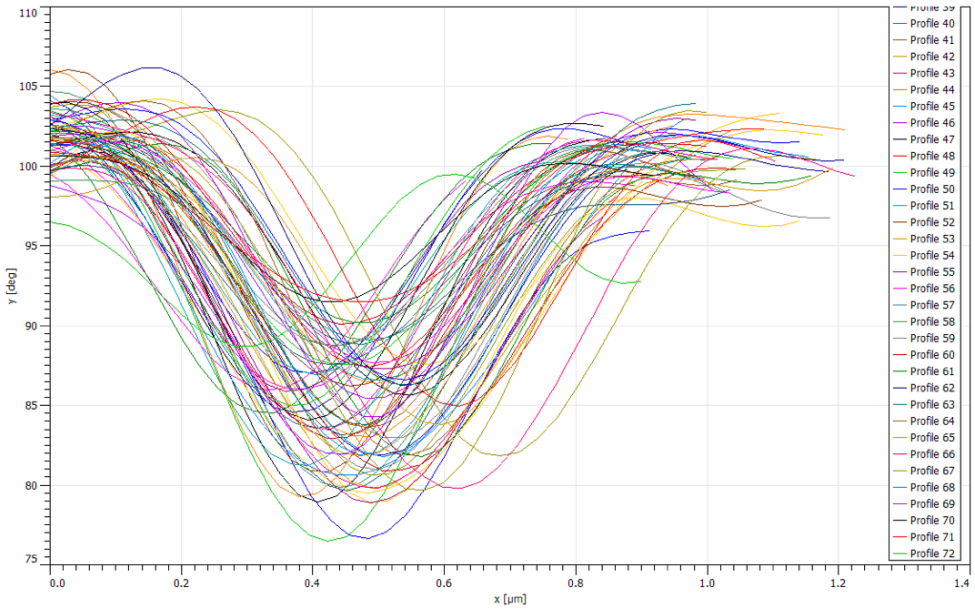

Figure 39: The curves are the sections of the vortices in the a) image of fig.38. Every curve was fitted with a gaussian function to extract the FWHM value.

For EP Niobium samples were collected 4 images at different scan heights. Multiple vortices are visible on the images, and also by eye is noticeable that the vortex profile becomes wider as scan height increases. To analyze datas quantitatively, some sections of the 2D vortices were taken (lines in fig.38) and the Full Width at Half Maximum (FWHM) of every profile (fig.39) was extracted with a gaussian fit. In fig.40 are reported the mean values of the FWHM for every scan height with errors.

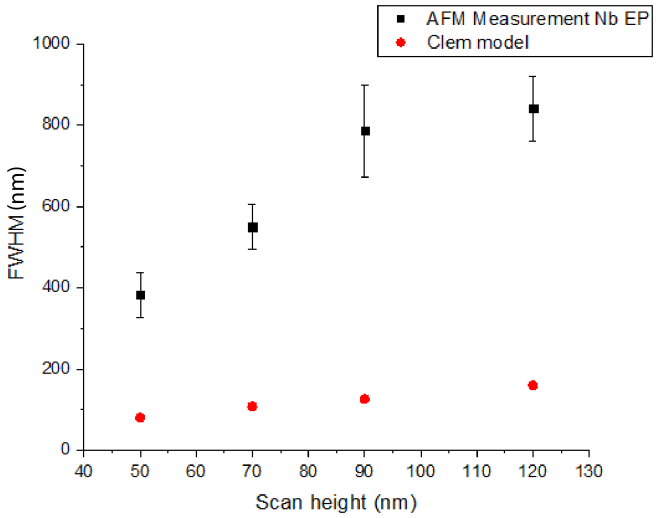

Figure 40: In the graph are reported in black the mean values and errors of the vortices's FWHMs in fig.38. There is a clear trend of growth of FWHM increasing the MFM scan height. In red are reported the values of FWHM calculated with the model, the trend is similar but there is a systematic shift of all points at lower FWMH.

There is a visible growing trend in function of the scan height. The model used for simulate the vortex profile is the Clem's model[3], and the sample-tip interaction was described in point dipole approximation. The MFM images are constructed with the phase difference between the driving force that keep the tip oscillating and the real oscillation of the tip:

$$\Delta\phi = -\frac{Q}{k}\frac{\partial F_z}{\partial z} \tag{13}$$

where $Q = \Delta f/f_0$ is the quality factor of the oscillating tip, k is the Hooke constant of the harmonic oscillator and F_z is the force acting on the tip in z direction (perpendicular to the sample). The force components in the plane of the sample were neglected[10]. To connect the phase variation to the magnetic field we use the magnetic energy:

$$F_z = \frac{\partial E_{tip-sample}}{\partial z} \qquad\qquad E_{tip-sample} = m_{tip}B_z \tag{14}$$

where m_{tip} is the magnetization of the tip. So we obtain:

$$\Delta\phi = -\frac{Qm_{tip}}{k}\frac{\partial^2 B_z}{\partial z^2} \tag{15}$$

A form of B_z and its second derivative is obtained with the Clem model, solving the London equation for a superconducting half space (very thick film) the following relation is obtained[11]:

$$\frac{\partial^2 B_z(z,r)}{\partial z^2} = \frac{\phi_0}{2\pi\lambda^2}\int_0^\infty dk \frac{k^3 J_0(kr)}{k^2+\lambda^{-2}} \frac{\sqrt{k^2+\lambda^{-2}}}{k+\sqrt{k^2+\lambda^{-2}}} e^{-kz} \tag{16}$$

where λ is the London penetration depth, k is a wave vector resulting from a Fourier transform, z in the axes perpendicular to the sample's surface, r is the distance from the vortex core and $J_0(kr)$ is the zero order Bessel function with kr as argument.

The integral in eq.16 was numerically computed with Mathematica and in fig.40 are reported the calculated values at different scan height. The values were normalized to 1 because we are not interested in absolute values of phase variation but just relative values in r direction. In fig.41 the computed and the measured values are compared, the growing trend is reproduced but the FWHM are not in agreement. The explanation is that the model used is too much simplified, the tip was considered to be a magnetic dipole but this is a gross approximation[12]. In fact an MFM image is the convolution between the the magnetic properties of the sample and the tip. The tip has a finite volume and therefore considering it a point is an approximation and comports a underestimation of the vortex FWHM value.

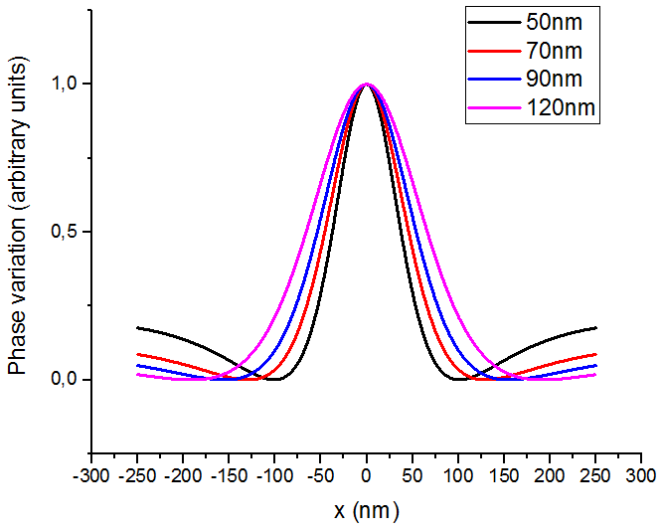

Figure 41: In the graph is reported the phase variation calculated with the Clem model considering the tip a point magnetic dipole. The data were normalized in phase because in this study we look only at relative variations in x direction (in the plane of the sample). There is a growth of the FWHM with increasing MFM scan height.

In fig.42 is reported the MFM image of the 1000^{o}C 10 mTorr 2h sample at 70 nm scan height. The vortices FWHMs were measured and the mean value is 1,2 μm, that is double of the FWHM value at the same scan height for EP Nb. This means that the MFM technique is sensible to the surface structure of the material and with a good model is possible to estimate properties of the surface.

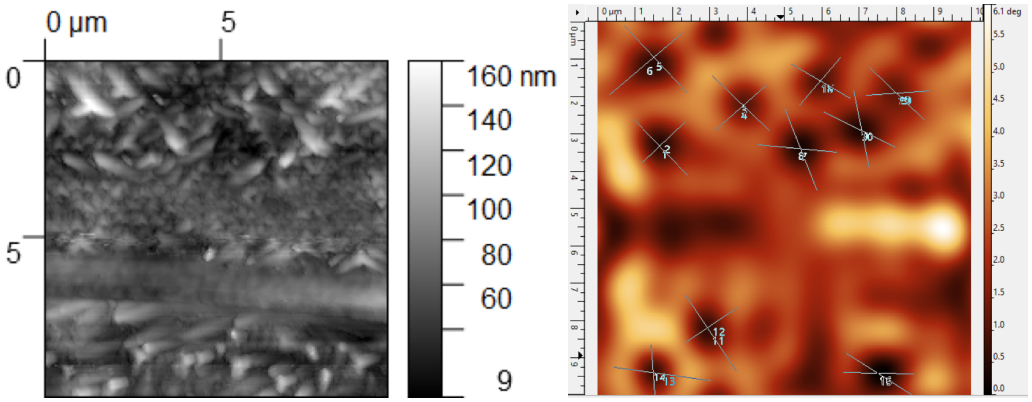

Figure 42

6 Conclusions

6.1 NbN synthesis

In literature the niobium nitride formation is studied prevalently at high temperature ($1700 - 2000^oC$) and high pressure (1-300 bar)[7,13–15]. Our final task is to do the treatment on niobium cavities that can't be treated at so high temperatures (the mechanical properties change too much and deformations can occur) and we have to use a big furnace that can't reach so high pressure of nitrogen. Than we chose to work in another zone of the phase diagram, where the conditions are more suitable to treat cavities. This low temperature-low pressure zone of the phase diagram is not well studied. As a starting point we extrapolated the working parameters from an empiric relation calculated for higher temperatures. We performed the treatment on two samples and we obtained the SEM evidence of a $1\mu m$ thick layer different from bulk. However we didn't be able to find out the composition with EDX, for the too low sensitivity to nitrogen. To know more about the surface composition SIMS measurements should be done. For what concerns the superconducting properties, we didn't find any transition of common nitride phases (12-17K) but we've found a transition at 8,33 K that is different from all the common nitride phases and could be a new superconducting NbN phase. So, in conclusion, might be interesting to study the low temperature of the NbN phase diagram to know more about the stable phases and the conditions of stability.

6.2 Vortices study

MFM is a good method to map vortices, the main advantage is that the FWHM depends strongly on surface London penetration depth. This is evident comparing the vortex profile width of EP Nb and the one of treated Nb, changing the surface structure (adding impurity) the width doubles. To do quantitative analysis of the images the simple point-dipole interaction model is too rough. In fact the MFM images are always a convolution of tip's and sample's magnetic moment. A real tip is not a point and can present multipole components of the magnetization not only in z direction but also in the sample's surface plane. So can be interesting to develop a more sophisticated model to describe the tip and to fit the vortex profile calculating the surface London penetration depth and other surface properties.

References

[1] M. Checchin, *PhD thesis*, Illinois Institute of Technology, 2016.

[2] J. F. Annett, *Superconductivity, Superfluids and Condensates*, OUP Oxford, 2004.

[3] R. Hubener, *Magnetic Flux Structures in Superconductors*, Springer, 1979.

[4] attocube, *User Manual Atomic Force Microscope attoAFM/MFM Ixs*, october 2014 edn.

[5] Quantum Design, *Physical Property Measurement System (Hardware Manual)*.

[6] Quantum Design, *VIBRATING SAMPLE MAGNETOMETER (Brochure)*.

[7] M. Joguet, W. Lengauer, M. Bohn and J. Bauer, *Journal of Alloys and Compounds*, 1998, **269**, 233 – 237.

[8] A. H. Farha, A. O. Er, Y. Ufuktepe, G. Myneni and H. E. Elsayed-Ali, *Surface and Coatings Technology*, 2011, **206**, 1168 – 1174.

[9] O. M. A. R. Y. Trenikhina, A. Grassellino, author, 2015.

[10] U. Hartmann, *Phys. Lett. A*, 1989, **137**, 475–478.

[11] G. Carneiro and E. H. Brandt, *Phys. Rev. B*, 2000, **61**, 6370–6376.

[12] E. Nazaretski, J. P. Thibodaux, I. Vekhter, L. Civale, J. D. Thompson and R. Movshovich, *Applied Physics Letters*, 2009, **95**, 262502.

[13] V. Buscaglia, F. Caracciolo, M. Ferretti, M. Minguzzi and R. Musenich, *Journal of Alloys and Compounds*, 1998, **266**, 201 – 206.

[14] A. Linde, R.-M. Marin-Ayral, D. Granier, F. Bosc-Rouessac and V. Grachev, *Materials Research Bulletin*, 2009, **44**, 1025 – 1030.

[15] W. Lengauer, M. Bohn, B. Wollein and K. Lisak, *Acta Materialia*, 2000, **48**, 2633 – 2638.